Tunable correlated-electron phases in (111) $LaAlO_3/SrTiO_3$ band insulator heterostructures

Juan Ignacio Beltrán[1,2] and M. Carmen Muñoz[1,*]

[1]*Instituto de Ciencia de Materiales de Madrid, ICMM-CSIC, Cantoblanco, 28049 Madrid, Spain*

[2]*GFMC, Departamento de Física de Materiales, Universidad Complutense de Madrid, 28040 Madrid, Spain*

(Received 31 January 2017; revised manuscript received 26 May 2017; published 16 June 2017)

Density functional theory calculations reveal the existence of different correlated-electron ground states in (111)-oriented *n*-type $LaAlO_3/SrTiO_3$ symmetric superlattices. They can be tuned by selecting the $SrTiO_3$ thickness, and range from a trivial metal for thick $SrTiO_3$ slabs to a Mott-type antiferromagnet in the ultrathin limit. An itinerant ferromagnet and a half-metal phase are also stable in the intermediate region. This remarkable property is a distinct characteristic of (111) perovskite heterostructures and originates from the combined effect of polar discontinuity at the interface, trigonal lattice symmetry, and quantum confinement. While the polar discontinuity promotes the filling of the empty *d* states of the $SrTiO_3$ with one electron, the trigonal symmetry dictates that the wave function of the occupied bands spreads over the entire $SrTiO_3$ slab. Thus, the electron density can be chosen by selecting the number of $SrTiO_3$ layers. For high densities, symmetry breaking and on-site Coulomb interaction drive the occurrence of correlated-electron ground states. Our results show that low dimensionality can lead to unconventional behavior of oxide heterostructures formed by electronically fairly simple nonmagnetic band insulators, and can open perspectives for the use of $LaAlO_3/SrTiO_3$ superlattices grown along the [111] direction to explore quantum phase transitions.

DOI: 10.1103/PhysRevB.95.245120

I. INTRODUCTION

Complex oxide heterostructures (HSs) offer the possibility of tuning crystal symmetry, strain, spatial confinement, and dimensionality and thereby they allow one to manipulate the charge, spin, and orbital order. Therefore, in atomically engineered oxide HSs new and unprecedented ground states emerge [1–3]. The prototypical example is (001)-oriented $LaAlO_3/SrTiO_3$ HSs formed by two nonmagnetic band insulators. In these HSs a high-mobility two-dimensional electron gas (2DEG), exhibiting metallic [4], magnetic and superconducting behavior, arises [5–10]. The polar discontinuity at the interface is primarily considered to drive the occurrence of the 2DEG [4,11,12], but oxygen vacancies [13–15], cation intermixing [11,12], and even surface protonation [16,17] also yield conductive HSs. It is widely accepted that the 2DEG is confined in the $SrTiO_3$ and, irrespective of the $SrTiO_3$ thickness, electrons mainly reside at the two-dimensional (2D) d_{xy} orbital of the interface TiO_2 plane. However, there is also some occupation of the d_{xy} noninterface TiO_2 and the 3D $d_{yz/zx}$ derived bands [18–23]. Additionally, ferromagnetism was predicted to be an intrinsic property of the 2DEG [23–26], associated with the Ti d_{xy} orbital, albeit some theoretical explanations have proposed an extrinsic origin [27]. Direct experimental evidence for Ti d_{xy} in-plane ferromagnetic order was later reported [28].

In sharp contrast to the universal metallic ground state of (001) $LaAlO_3/SrTiO_3$ HSs, here we describe the quantum mechanical design of an oxide HS able to exhibit different ground states. The key to designing such a system is to envisage a HS with a polar discontinuity at the interface to promote the confinement of net charge in one of its constituents and with a crystal symmetry yielding a quasi-uniform spatial charge distribution. Thus, by changing the thickness of the confinement material the electron density can be tailored. We prove that (111)-oriented $LaAlO_3/SrTiO_3$ superlattices (SLs) with symmetric LaO_3-Ti interfaces satisfy both constrains and exhibit different electronic phases depending on the $SrTiO_3$ thickness. The SL ground state evolves from a metallic nonmagnetic phase, to an itinerant ferromagnet, a half-metal, and finally to a Mott-type antiferromagnetic insulator as the $SrTiO_3$ thickness is reduced. The spatial dimension being therefore the macroscopic tuning parameter driving the quantum phase transitions. Figure 1 shows a schematic representation of the SLs phase diagram.

(111)-oriented perovskite HSs have been the subject of intensive research in recent years, motivated by the possibility of realizing topological phases and quantum many-body states. Novel topological phases were first predicted in (111) $LaAuO_3/LaAlO_3$ HSs [29] and subsequently in a (111) $LaAlO_3/SrTiO_3$ HS containing two Ti layers [30] and in the (111) bilayer of $LaNiO_3$ [31], among others systems. Moreover, a Mott insulator as well as an antiferromagnetic correlated ground state have also been predicted in (111) HSs involving strongly correlated oxides [32–35]. At present, the formation of a 2DEG has already been reported in (111)-oriented $LaAlO_3/SrTiO_3$ interfaces [36,37] and in the bare surface of (111) $SrTiO_3$ crystals [38,39]. Recently (111)-oriented perovskite SLs were synthesized [40,41].

II. MODEL AND METHOD

We focus on (111) $(LaAlO_3)_n/(SrTiO_3)_m$ (n/m) SLs with two identical LaO_3-Ti interfaces. n and m are the numbers of Al and Ti planes contained in the SL unit cell (u.c.), and consequently the SLs are formed by $n+0.5$ $LaAlO_3$ and $m-0.5$ $SrTiO_3$ u.c., respectively. Along the [111] direction, the SLs have threefold rotational symmetry and the SL crystal symmetry is trigonal if $(n+m) \neq 3N$ and hexagonal if $(n+m) = 3N$, N being an integer [42]. They consist of alternating planes of LaO_3 (SrO_3) and Al (Ti). Figure 1 shows the 3D structure of the (111) (5/4)

*mcarmen@icmm.csic.es

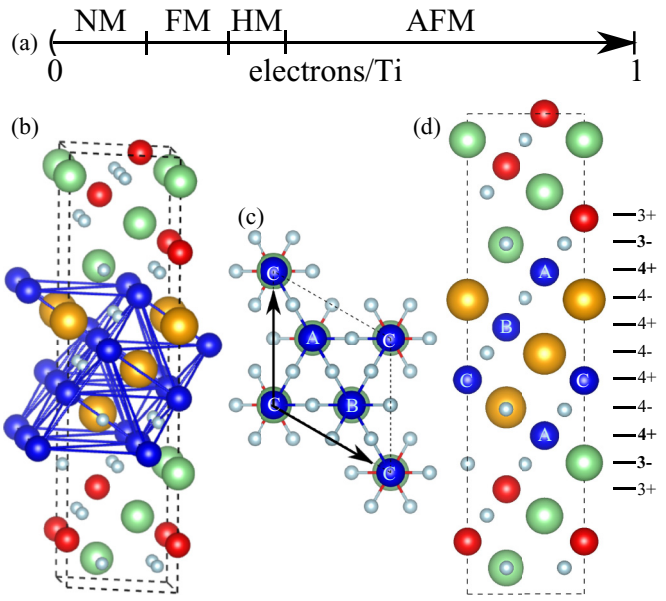

FIG. 1. (a) Schematic phase diagram of the $SrTiO_3$ accumulated charge as a function of the average linear electron density in the (111) Ti planes. NM, FM, HM, and AFM stand for nonmagnetic, itinerant ferromagnetic, half-metal, and antiferromagnetic phases, respectively. Different views of the 5/4 SL with two symmetric LaO_3-Ti interfaces: (b) tilted view, (c) (111), and (d) (11 −2) planes. Ti, Sr, Al, La, and O atoms correspond to dark-blue, golden, red, light-green and light-blue spheres, respectively. Dashed lines depict the SL u.c. and continuous lines the Ti-Ti bonds. The nominal ionic charges for the atomic planes along the [111] direction are given at the right of the figure.

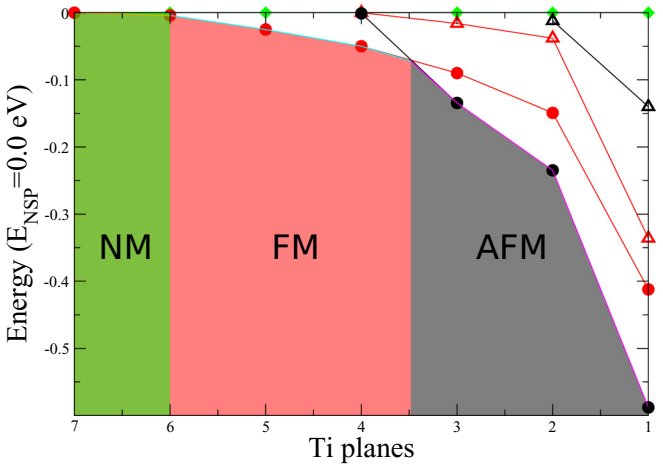

FIG. 2. Energy difference between the magnetic phases—ferromagnetic (red) and in-plane antiferromagnetic (black)—and the nonmagnetic (green) phase for $(LaAlO_3)_n/(SrTiO_3)_m$ SLs, as a function of the number of the Ti layers m in the $SrTiO_3$ slab. $n = 4$ or 5 and $n + m = 3N$, N being an integer, thus all the SLs have hexagonal symmetry. Circles correspond to calculations performed with $U - J = 4.3$ eV, while the triangles represent those with $U - J = 2.0$ eV.

SL. The Ti atoms in the (111) planes are second neighbors, forming a centered hexagonal 2D lattice, and following an A, B, and C stacking sequence. When only two Ti planes are considered, they form a buckled honeycomb lattice. All the alternating planes along the [111] direction are nominally highly charged: LaO_3^{3-} and Al^{3+} for $LaAlO_3$ and SrO_3^{4-} and Ti^{4+} for $SrTiO_3$, as illustrated in Fig. 1. This is in contrast to the [001] direction, where only the $LaAlO_3$ planes are charged while the $SrTiO_3$ layers are formally charge neutral. Despite their differences in stacking and nominal charge of the individual planes, a similar polar discontinuity arises at the n-type interfaces of both the (111) and (001) SL orientations.

Density functional theory (DFT) calculations were performed with a plane-wave basis set and the projector-augmented-wave method as implemented in the Vienna *Ab initio* Simulation Package, VASP [43,44]. For the exchange-correlation energy, we used the generalized gradient approximation (GGA) with the Perdew-Burke-Ernzerhof functional [45]. Static local electronic correlations were added and the GGA+ U potential is treated in the rotationally invariant form [46]. Most of the results discussed in the article were obtained with $U = 5$ eV, $J = 0.7$ eV for Ti $3d$ and $U = 11$ eV for La $4f$. These values of the Hubbard-like Coulomb interaction are widely accepted for the titanates and we have previously used them in the calculations of (001) $LaAlO_3/SrTiO_3$ SLs [23]. In addition, calculations with $U - J = 2$ and 6.5 eV for the Ti $3d$ have been performed. The electronic wave functions were represented in a plane-wave basis with the energy cutoff set at 500 eV.

Periodic boundary conditions were applied to a supercell containing $n + 0.5$ u.c. of $LaAlO_3$ on top of $m - 0.5$ u.c. of $SrTiO_3$. The in-plane lattice parameter, perpendicular to the [111] direction, was fixed to 5.52 Å, corresponding to the calculated equilibrium 3.905 Å bulk $SrTiO_3$ cubic lattice constant. This value is almost identical to the 3.897 Å experimental one. Full relaxations of the out-of-plane lattice parameter and of all the atomic positions were done until the force on each atom was below 0.01 eV/Å. To determine the magnetic ground state, we considered the collinear ferromagnetic (FM) and the two possible, interlayer and intralayer, antiferromagnetic (AFM) structures. In the intralayer AFM configuration, we doubled the in-plane u.c. and thus a $2 \times 1 \times (n + m)$ SL u.c. was used. Brillouin-zone (BZ) integrals were computed in a sufficiently dense k-point grid. We used a Γ-centered Monkhorst-Pack mesh sampling of $12 \times 12 \times 1$, and of $6 \times 12 \times 1$ for the 1×1 and 2×1 in-plane u.c., respectively.

III. VARIABLE GROUND STATES AS A FUNCTION OF THE $SrTiO_3$ THICKNESS

Figure 2 presents the dependence of the total energy of the different electronic phases on the $SrTiO_3$ thickness—number of Ti planes—for several $(LaAlO_3)_n/(SrTiO_3)_m$ SLs with hexagonal symmetry, $n + m = 3N$, N being an integer. In the large $SrTiO_3$ thickness limit—we performed calculations up to $m = 18$—for the widely accepted $U - J = 4.3$ eV value of the Hubbard-like on-site Coulomb interaction [23], the SL ground state is a trivial nonmagnetic metal. As the number of Ti planes decreases, a ferromagnetic phase stabilizes, while for $m \leqslant 3$ $SrTiO_3$ slab thicknesses an in-plane antiferromagnetic symmetry broken ground state emerges. The energy differences between the magnetic and nonmagnetic phases are

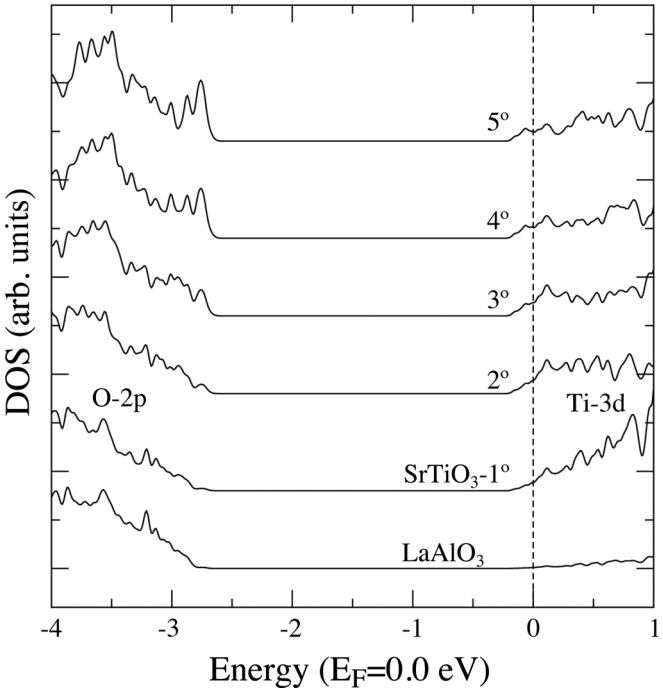

FIG. 3. Layer projected total DOS around the bulk $SrTiO_3$ energy gap for the 5/10 SL; only half of the Ti and the first Al atomic planes of the SL u.c. are represented. The energy zero corresponds to the Fermi level.

particularly large in the ultrathin $SrTiO_3$ limit, although they are reduced as the number of Ti layers increases. Therefore, the SL ground state depends on the number of Ti planes.

Figure 3 shows the layer projected density of states (LDOS) for the nonmagnetic 5/10 SL. As expected, net charge accumulates in the $SrTiO_3$ slab to screen the polar discontinuity at the interfaces. The SL is metallic, and the Fermi level, E_F, lies close to the bottom of the SL conduction band (CB) formed by Ti derived t_{2g} d bands. The total charge, calculated by integrating the total DOS for all the occupied CB states bellow E_F, is equal to 1, as dictated by the nominal polar discontinuity; each interface contributes 0.5 electrons. Hence, one electron is confined in the $SrTiO_3$ slab.

The CB dispersion relations for the ground state of several representative n/m SLs, where $n = 4$ or 5 while m ranges from 10 to 1, are shown in Fig. 4. The corresponding spin-resolved total DOSs are also depicted. The trigonal C_{3v} lattice symmetry of the (111) SLs breaks the orbital threefold t_{2g} degeneracy of $3d$ Ti states and introduces additional level splitting into an a_{1g} and two e'_{2g} bands [47]. In all the SLs, the lowest-lying energy subband corresponds to the a_{1g}, and the energy splitting between a_{1g} and e'_{2g} increases as the $SrTiO_3$ thickness is reduced. The dispersion relations reflect the subband quantization generated by the finite size of the $SrTiO_3$.

A. Metallic and magnetic phases

For SLs with $m > 3$ the Fermi level lies within the Ti-derived CB, corresponding to a metallic ground state. In addition, for $m \leqslant 6$ the spin-symmetry is broken and a spontaneous Zeeman-like exchange splitting, which increases as m decreases, arises. Hence, as the total charge accumulated in the CB for all the SLs is equal to one electron, the number of $SrTiO_3$ layers determines the band filling and accordingly the SL ground state evolves from a nonmagnetic metal for thick $SrTiO_3$ slabs to a spontaneous ferromagnet, and at $m = 4$ to a half-metal state with 100% spin polarization.

Figure 5 represents the evolution of the total magnetic moment with the width of the $SrTiO_3$ slab for the magnetic phases of the $(LaAlO_3)_n/(SrTiO_3)_m$ SLs. For $m = 7$ a significant spontaneous magnetic moment develops, although the energies of the ferromagnetic and non-magnetic phases are almost identical. However, as the $SrTiO_3$ thickness decreases, the ferromagnetic phase has the lowest energy and the total magnetic moment steadily increases, reaching $1\mu_B$ for $m = 4$.

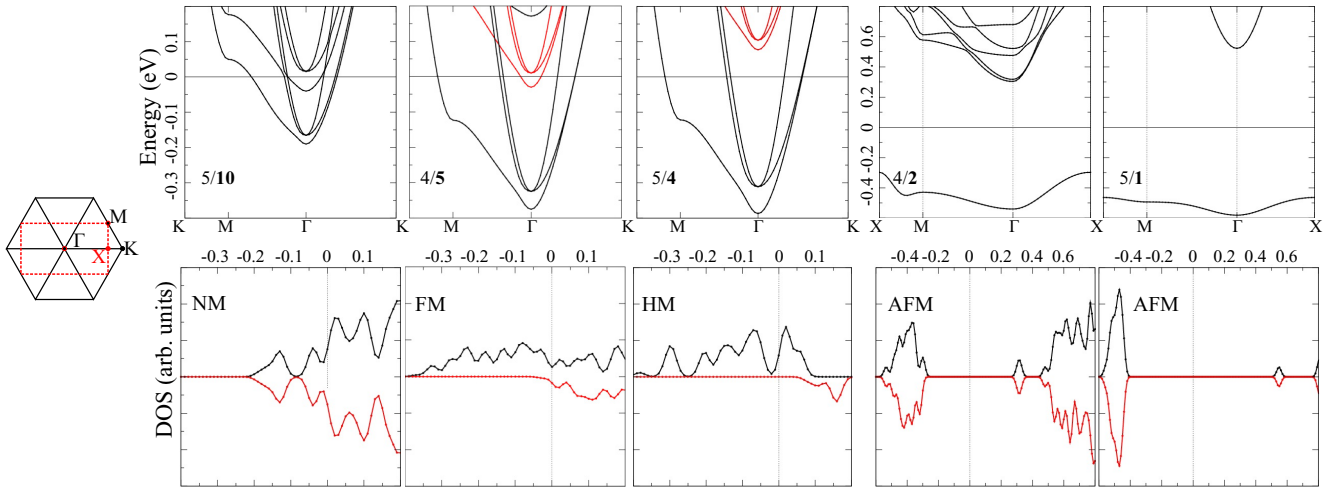

FIG. 4. Spin resolved conduction band for several representative SLs: from left to right, 5/10, 4/5, 5/4, 4/2, and 5/1 SLs. The corresponding DOSs are shown at the bottom. Black and red lines are majority and minority spin states, respectively. The energy zero coincides with E_F in metallic SLs and separates occupied from unoccupied states in the insulator SLs. On the left are the in-plane BZs for metallic SLs containing one (black) and for insulator SLs with two (red) Ti atoms per plane. The BZ of metallic SLs is hexagonal for $n + m = 3N$, N being an integer, and trigonal for $n + m \neq 3N$.

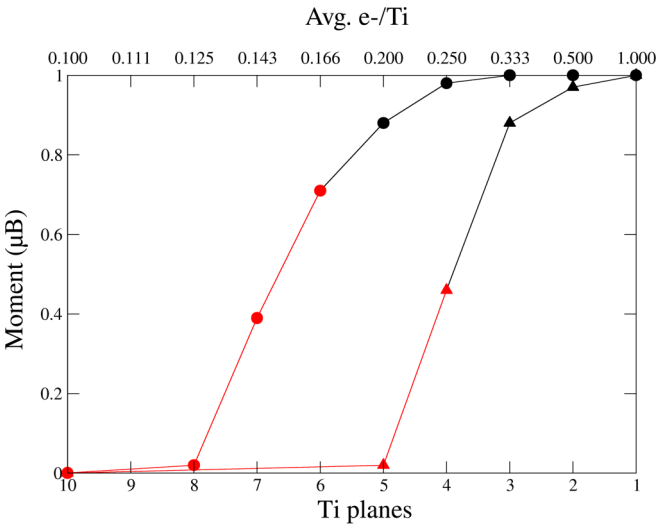

FIG. 5. Total magnetic moment versus the number of Ti planes m, for the magnetic phases of $(LaAlO_3)_n/(SrTiO_3)_m$ SLs; m ranges from 1 to 10, $n = 4$ or 5, and $n + m = 3N$. For the AFM $m \leqslant 3$ SLs the displayed magnetic moments are those of a single Ti, since the total moment is zero. Black points correspond to SLs with a magnetic ground state, while red points represent the magnetic moment of SLs whose ferromagnetic phase has an energy similar or slightly larger than that of the nonmagnetic phase.

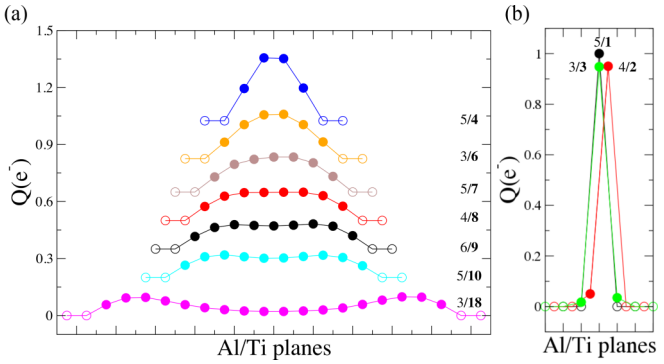

FIG. 7. Charge density profile for n/m SLs, where m ranges between 18 and 1; left panel $18 \geqslant m \geqslant 4$ and right panel $3 \geqslant m \geqslant 1$. The figure display the spatial distribution of the CB charge. Full and empty points correspond to Ti and Al planes, respectively.

As Figure 4 shows, the decrease of the $SrTiO_3$ thickness yields larger a_{1g}-e'_{2g} energy splitting and the lifting of the spin-degeneracy for the narrower cases. There is an almost rigid shift between the a_{1g} and e'_{2g} subbands as well as between the majority and minority spin states. Therefore, the subband dispersions are similar for all the metallic SLs and the estimated effective masses from the calculated dispersion relations are $0.70m_e$ and $1.30m_e$ for a_{1g} and $0.90m_e$ and $0.45m_e$ for e'_{2g} along the Γ-K and Γ-M directions, respectively. They compare with 0.70 and 0.45 for bulk $SrTiO_3$ along the same crystallographic directions. The observed rigid band shift results in different occupations of similar subbands in SLs with different numbers of $SrTiO_3$ layers and determines the SL Fermi surfaces (FSs). This is clearly evidenced in Fig. 6, which shows the $k_z = 0$ plane in the center of SL hexagonal Brillouin zone of two illustrative examples, the 5/10 and the 4/5 SLs. The band dispersion along the perpendicular Γ-A direction is very small and therefore the band structure is quasi-two-dimensional. The 5/10 SL is nonmagnetic while the 4/5 SL is a metal ferromagnet and thus the FS is spin-polarized. The FS of the 5/10 SL is formed by four closed sheets: the smallest almost circular electron pocket around the Γ point arises from the second quantized occupied a_{1g} subband while the first quantized t_{2g} subbands yield two isotropic e'_{2g} electron pockets—the inner one being also almost an ideal circle–and an outer highly anisotropic a_{1g} sheet, with extrema in the Γ-M direction. The majority 4/5 FS is equivalent although only the three sheets arising from the first quantized t_{2g} subbands are present. In addition, due to the lower subband occupation—see Fig. 4—the a_{1g} sheet is open and there is a neck around M. A small almost circular electron pocket accounts for the 4/5 minority FS. Hence, the FSs of SLs with different periods are unlike, despite corresponding to energy cuts of similar dispersion bands.

As previously stated, the polar discontinuity at the interfaces dictates that one electron is confined in the SL CB. However, its spatial distribution is enforced by the lattice geometry and therefore by the wave function symmetry of the a_{1g} and e'_{2g} bands. Figure 7(a) illustrates the CB spatial charge distribution for SLs with different periods. The electron is fully confined in the $SrTiO_3$ slab, and up to $m = 10$ it is almost homogeneously distributed. Only in the long-range limit, where higher-order quantized subbandas are occupied, does the electronic charge tends to accumulate towards the interfaces; see the charge distribution of the $m = 18$ SL. The

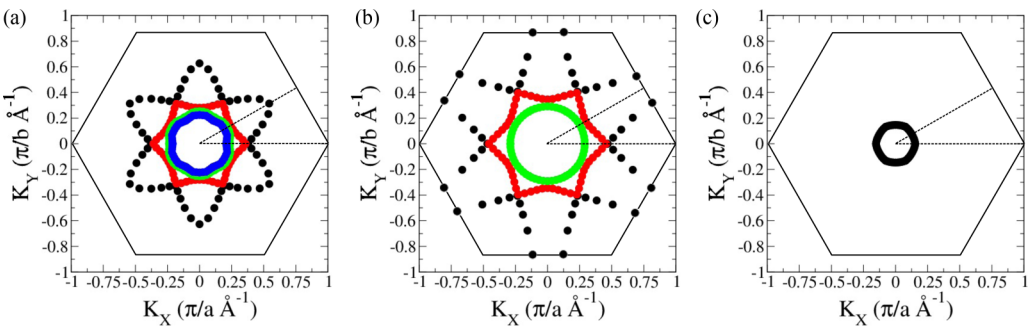

FIG. 6. Fermi surface at the $kz = 0$ plane of the 5/10 (a), majority spin 4/5 (b) and minority spin 4/5 (c) SLs.

homogeneous spatial distribution results in an almost linear dependence on $1/m$ of the electron density, which increases by more than a factor of 3 in the $10 \geqslant m \geqslant 3$ range, i.e, from 0.1 to 0.33 electrons/Ti. Therefore, the reduction of m results in the increase of the electron density and, since Coulomb interactions are more important at higher densities, it leads to the enhancement of the effective electronic correlation. This effect, originated by the symmetry of the (111) SLs, explains the occurrence of distinct correlated quantum states for SLs with different m and the emergence of ground states associated with stronger electron-electron interactions for smaller m values.

B. Mott-like insulator phase

In principle, short-range Coulomb interactions should dominate in the ultrathin limit $m \leqslant 3$, where the electron density approaches the extreme limit. The right panels of Fig. 4 show the dispersion relation for the $m = 1$ and 2 SLs. In these SLs the electron resides solely in the anisotropic a_{1g} subband. There is a drastic increase of its effective mass, particularly in the Γ-M direction, and a large gap between the a_{1g} and e'_{2g} subbands opens up. Both, the mass enhancement and the energy gap are larger for $m = 1$. Hence, although these SLs hold a polar induced electron in their CB, they are insulators. Furthermore, for $m = 2$ and 3 the emergence of the energy gap is linked to charge disproportionation, as the right panel of Fig. 7 displays: the electron is not shared equally by all the Ti planes but it is mostly confined in a single atomic layer. Hence the ground state is charge ordered. In addition, in all the insulator SLs, $m \leqslant 3$, in-plane antiferromagnetic order stabilizes; see Fig. 2. Therefore, these SLs—with one electron per Ti plane—exhibit a huge charge density $\approx 6.6 \times 10^{14}$ cm^{-2}, and the CB charge is commensurate with the underlying lattice. Consequently, for $m \leqslant 3$ a ground state corresponding to strong electron-electron interaction arises. The SLs exhibit a Mott-type insulator phase and the electron, residing at a single Ti orbital, switches from the itinerant to the localized regime.

In Fig. 5 the magnetic moments of a single Ti atom for n/m SLs, $m \leqslant 3$, are also displayed. Since the total charge—one electron—is located at a single Ti orbital and the SLs exhibit in-plane AFM order, the magnetic moment is equal to $1\mu_B$ per Ti atom, and the total magnetic moment is zero.

Thus, as a consequence of the combined effects of polar discontinuity and wave function symmetry a new emergent strongly correlated state is sustained by the ultrathin $(LaAlO_3)_n/(SrTiO_3)_m$ SLs.

IV. CONFINEMENT, LATTICE DISPLACEMENT, AND ELECTRONIC CORRELATIONS

The stabilization of different ground states is achieved by changing the number of layers of the $SrTiO_3$ slab. In contrast, variations of the $LaAlO_3$ thickness do not alter the conducting or magnetic nature of the SL whenever $n \geqslant 3$, and thus the $LaAlO_3$ energy gap is close to the bulk value. The role of the $LaAlO_3$ slab is to provide the polar discontinuity at the interface and the staggered energy gap that promotes the confinement of the polar induced charge in the $SrTiO_3$ constituent of the SL.

Furthermore, metallic SLs always show displacements of the oxygen atoms in the SrO_3 planes, with two and one oxygen moving inwards and upwards $\approx \pm 0.04$ Å along the [111] direction, respectively. In the thick $SrTiO_3$ limit, $m \geqslant 10$, the distortions are restricted to the planes close to the interfaces. Moreover, for ultrathin AFM insulator SLs unequal O-Ti bonds within an octahedron fluctuate around 2.00 ± 0.04 Å. Nevertheless, neither the displacements of the oxygen atoms nor the distortions of the Ti-O bonds alter the ferromagnetic or the conducting nature of the SL ground state. These results are in contrast to those found in the (100) $LaAlO_3/SrTiO_3$ SLs, where the displacement of the oxygen atoms promotes the appearance of a magnetic ground state [23]. The different behavior of both orientations is due to the different orbital character of the confined charge in the $SrTiO_3$, which is always multiorbital in (111) SLs while in the (100) SLs the occupation of the $d_{yz/zx}$ bands is induced by the ferroelectric-like distortions of the TiO_6 octahedra. This finding supports the fact that the multiorbital character of the accumulated electron charge is an essential ingredient to promote ferromagnetism, as has already been proposed [23,26,32].

The results discussed so far correspond to calculations performed with $U - J = 4.3$ eV, a widely accepted Hubbard-like on-site Coulomb interaction for the titanates [23]. For smaller $U - J$ the nonmagnetic phase is favored. For example, Fig. 2 also displays for $U - J = 2$ eV the total energy of the different electronic phases versus the number of Ti planes. The ferromagnetic phase is stable against room temperature thermal fluctuations only in the ultrathin limit up to $m = 3$, and the n/m SLs are nonmagnetic for larger m. Moreover, the strongly correlated Mott phase is not stable at any m, since it always has higher energy, and even in the extreme-thin limit, $m = 1$, the metallic ferromagnetic phase is the ground state. In contrast, for a very large value $U - J = 6.5$ eV—not shown in the figure—the Mott-type AFM insulator phase corresponds to the ground state even for $m = 4$. Furthermore, for a given $SrTiO_3$ thickness, the magnetic moment also depends on the value of the Hubbard-like interaction and it is always smaller for smaller $U - J$. In Fig. 5 the magnetic moments of n/m SLs calculated with $U - J = 2$ eV are also displayed. All of them are smaller than those obtained for the same m with higher $U - J$. Note that all the magnetic SLs are ferromagnetic.

Consequently, the critical $SrTiO_3$ thicknesses for the occurrence of a specific quantum phase transition do depend on the Coulomb repulsion. These results provide evidence of the significant role of electron-electron interaction in the emergence of strongly correlated phases in the SLs. The predicted quantum phase transitions as a function of the $SrTiO_3$ thickness are a nontrivial consequence of enhanced electron correlation due to quantum confinement in a trigonal lattice.

For (111) $LaAlO_3/SrTiO_3$ HSs containing a Ti bilayer, the emergence of a topologically nontrivial phase had been predicted. The topological phase corresponds to the inversion symmetric CB state, where the electron is equally shared by the two Ti planes [30]. We found that the symmetric state has 160 meV higher energy than the Mott-type AFM ground state solution discussed above. Indeed, the largest energy difference

among different phases for a given SL corresponds to SLs in the ultrathin limit, $m \leqslant 3$, see Fig. 2.

V. SUMMARY AND CONCLUSIONS

In summary, our results provide evidence that the combined effects of the polar discontinuity and the underlying C_{3v} lattice symmetry of (111)-oriented transition-metal oxide perovskite HSs contribute to the realization of a variety of unique and singular ground states. In symmetric n-type (111) $LaAlO_3/SrTiO_3$ superlattices there is a single electron quasi-uniformly confined in the entire $SrTiO_3$ slab. Thus, by selecting the $SrTiO_3$ thickness, the electron density and in turn the effective electron correlation can be chosen. As the $SrTiO_3$ thickness is reduced the SLs evolve from a nonmagnetic itinerant metal, similar to doped (111) $SrTiO_3$ surfaces, towards the strongly correlated AFM Mott insulator state with one electron in a single Ti atom. For intermediate densities, an itinerant ferromagnet and a half-metal phase stabilize. The renormalization of the effective electron correlation is a nontrivial consequence of quantum confinement in systems with trigonal lattice symmetry. Therefore, (111) $LaAlO_3/SrTiO_3$ SLs can be grown with a tailored conducting and magnetic ground state. In the extreme limit of quantum confinement a robust Mott insulator can be synthesized from the combination of noncorrelated band insulator oxides. Accordingly, (111) $LaAlO_3/SrTiO_3$ superlattices are ideal systems to investigate quantum phase transitions into a variety of singular ground states.

ACKNOWLEDGMENTS

This work has been supported by the Spanish Ministry of Economy and Competitiveness through MINECO/FEDER Grants No. MAT2015-66888-C3-1R and No. 3R. The use of computational resources of CESGA is acknowledged.

[1] N. M. Nemes, M. J. Calderón, J. I. Beltrán, F. Y. Bruno, J. García-Barriocanal, Z. Sefrioui, C. León, M. García-Hernández, M. C. Muñoz, L. Brey, and J. Santamaría, Adv. Mater. **26**, 7516 (2014).

[2] C. A. Jackson, J. Y. Zhang, C. R. Freeze, and S. Stemmer, Nat. Commun. **5**, 4258 (2014); S. Raghavan, J. Zhang, and S. Stemmer, Appl. Phys. Lett. **106**, 132104 (2015).

[3] Y. Cao, X. Liu, M. Kareev, D. Choudhury, S. Middey, D. Meyers, J.-W. Kim, P. J. Ryan, J. W. Freeland, and J. Chakhalia, Nat. Commun. **7**, 10418 (2016).

[4] A. Ohtomo and H. Y. Hwang, Nature (London) **427**, 423 (2004).

[5] N. Reyren, S. Thiel, A. D. Caviglia, L. F. Kourkoutis, G. Hammerl, C. Richter, C. W. Schneider, T. Kopp, A.-S. Retschi, D. Jaccard *et al.*, Science **317**, 1196 (2007).

[6] A. Brinkman, M. Huijben, M. van Zalk, J. Huijben, U. Zeitler, J. C. Maan, W. G. van der Wiel, G. Rijnders, D. H. A. Blank, and H. Hilgenkamp, Nat. Mater. **6**, 493 (2007).

[7] Ariando, X. Wang, G. Baskaran, Z. Q. Liu, J. Huijben, J. B. Yi, A. Annadi, A. R. Barman, A. Rusydi, S. Dhar *et al.*, Nat. Commun. **2**, 188 (2011).

[8] D. A. Dikin, M. Mehta, C. W. Bark, C. M. Folkman, C. B. Eom, and V. Chandrasekhar, Phys. Rev. Lett. **107**, 056802 (2011).

[9] L. Li, C. Richter, J. Mannhart, and R. C. Ashoori, Nat. Phys. **7**, 762 (2011).

[10] J. A. Bert, B. Kalisky, C. Bell, M. Kim, Y. Hikita, H. Y. Hwang, and K. A. Moler, Nat. Phys. **7**, 767 (2011).

[11] N. Nakagawa, H. Y. Hwang, and D. A. Muller, Nat. Mater. **5**, 204 (2006).

[12] M. P. Warusawithana, C. Richter, P. Roy, J. A. Mundy, J. Ludwig, S. Paetel, T. Heeg, A. A. Pawlicki, L. F. Kourkoutis, M. Zheng, M. Lee, B. Mulcahy, W. Zander, Y. Zhu, J. Schubert, J. N. Eckstein, D. A. Muller, C. S. Hellberg, J. Mannhart, and D. G. Schlom, Nat. Commun. **4**, 2351 (2013).

[13] G. Herranz, M. Basletić, M. Bibes, C. Carrétéro, E. Tafra, E. Jacquet, K. Bouzehouane, C. Deranlot, A. Hamzić, J.-M. Broto, A. Barthélémy, and A. Fert, Phys. Rev. Lett. **98**, 216803 (2007).

[14] Z. Q. Liu, C. J. Li, W. M. Lü, X. H. Huang, Z. Huang, S. W. Zeng, X. P. Qiu, L. S. Huang, A. Annadi, J. S. Chen, J. M. D. Coey, T. Venkatesan, and Ariando, Phys. Rev. X **3**, 021010 (2013).

[15] L. Yu and A. Zunger, Nat. Commun. **5**, 5118 (2014).

[16] P. Scheiderer, F. Pfaff, J. Gabel, M. Kamp, M. Sing, and R. Claessen, Phys. Rev. B **92**, 195422 (2015).

[17] K. A. Brown, S. He, D. J. Eichelsdoerfer, M. Huang, I. Levy, H. Lee, S. Ryu, P. Irvin, J. Mendez-Arroyo, C. B. Eom, C. A. Mirkin, and J. Levy, Nat. Commun. **7**, 10681 (2016).

[18] M. Salluzzo, J. C. Cezar, N. B. Brookes, V. Bisogni, G. M. De Luca, C. Richter, S. Thiel, J. Mannhart, M. Huijben, A. Brinkman *et al.*, Phys. Rev. Lett. **102**, 166804 (2009).

[19] M. Sing, G. Berner, K. Go, A. M uller, A. Ruff, A. Wetscherek, S. Thiel, J. Mannhart, S. A. Pauli, C. W. Schneider *et al.*, Phys. Rev. Lett. **102**, 176805 (2009).

[20] Z. S. Popović, S. Satpathy, and R. M. Martin, Phys. Rev. Lett. **101**, 256801 (2008).

[21] M. Stengel, Phys. Rev. Lett. **106**, 136803 (2011).

[22] P. Delugas, A. Filippetti, V. Fiorentini, D. I. Bilc, D. Fontaine, and P. Ghosez, Phys. Rev. Lett. **106**, 166807 (2011).

[23] J. C. Li, J. I. Beltrán, and M. C. Muñoz, Phys. Rev. B **87**, 075411 (2013).

[24] R. Pentcheva and W. E. Pickett, Phys. Rev. B **74**, 035112 (2006).

[25] G. Chen and L. Balents, Phys. Rev. Lett. **110**, 206401 (2013).

[26] N. Ganguli and P. J. Kelly, Phys. Rev. Lett. **113**, 127201 (2014).

[27] N. Pavlenko, T. Kopp, E. Y. Tsymbal, G. A. Sawatzky, and J. Mannhart, Phys. Rev. B **85**, 020407 (2012).

[28] J.-S. Lee, Y. W. Xie, H. K. Sato, C. Bell, Y. Hikita, H. Y. Hwang, and C.-C. Kao, Nat. Mater. **12**, 703 (2013).

[29] D. Xiao, W. Zhu, Y. Ran, N. Nagaosa, and S. Okamoto, Nat. Commun. **2**, 596 (2011).

[30] D. Doennig, W. E. Pickett, and R. Pentcheva, Phys. Rev. Lett. **111**, 126804 (2013).

[31] K.-Y. Yang, W. Zhu, D. Xiao, S. Okamoto, Z. Wang, and Y. Ran, Phys. Rev. B **84**, 201104(R) (2011).

[32] R. Chen, S. B. Lee, and L. Balents, Phys. Rev. B **87**, 161119(R) (2013).

[33] D. Doennig, W. E. Pickett, and R. Pentcheva, Phys. Rev. B **89**, 121110(R) (2014).

[34] D. Puggioni, G. Giovannetti, M. Capone, and J. M. Rondinelli, Phys. Rev. Lett. **115**, 087202 (2015).

[35] S. Middey, D. Meyers, D. Doennig, M. Kareev, X. Liu, Y. Cao, Z. Yang, J. Shi, L. Gu, P. J. Ryan, R. Pentcheva, J. W. Freeland, and J. Chakhalian, Phys. Rev. Lett. **116**, 056801 (2016).

[36] G. Herranz, F. Sánchez, N. Dix, M. Scigaj, and J. Fontcuberta, Sci. Rep. **2**, 758 (2012).

[37] L. Miao, R. Du, Y. Yin, and Q. Li, Appl. Phys. Lett. **109**, 261604 (2016).

[38] S. McKeown Walker, A. de la Torre, F. Y. Bruno, A. Tamai, T. K. Kim, M. Hoesch, M. Shi, M. S. Bahramy, P. D. C. King, and F. Baumberger, Phys. Rev. Lett. **113**, 177601 (2014).

[39] T. C. Rödel, C. Bareille, F. Fortuna, C. Baumier, F. Bertran, P. Le Févre, M. Gabay, O. Hijano Cubelos, M. J. Rozenberg, T. Maroutian, P. Lecoeur, and A. F. Santander-Syro, Phys. Rev. Appl. **1**, 051002 (2014).

[40] D. Hirai, J. Matsuno, and H. Takagi, APL Mater. **3**, 041508 (2015).

[41] T. J. Anderson, S. Ryu, H. Zhou, L. Xie, J. P. Podkaminer, Y. Ma *et al.*, Appl. Phys. Lett. **108**, 151604 (2016).

[42] M. P. López Sancho, L. Chico, and M. C. Muñoz, Europhys. Lett. **40**, 679 (1997).

[43] G. Kresse and J. Hafner, Phys. Rev. B **47**, 558 (1993); G. Kresse and J. Furthmüller, *ibid.* **54**, 11169 (1996); G. Kresse and D. Joubert, *ibid.* **59**, 1758 (1999).

[44] P. E. Blöchl, Phys. Rev. B **50**, 17953 (1994).

[45] J. P. Perdew, K. Burke, and M. Ernzerhof, Phys. Rev. Lett. **77**, 3865 (1996); **78**, 1396 (1997).

[46] A. I. Liechtenstein, V. I. Anisimov, and J. Zaanen, Phys. Rev. B **52**, R5467 (1995); F. A. Vladimir, I. Anisimov, and A. I. Lichtenstein, J. Phys.: Condens. Matter **9**, 767 (1997).

[47] The a_{1g} and degenerate e'_{2g} bands are linear combinations of the three t_{2g} states, namely $\frac{1}{\sqrt{3}}(xy + yz + zx)$ for a_{1g} and $\frac{1}{\sqrt{3}}(xy + e^{\pm i\frac{2\pi}{3}} yz + e^{\mp i\frac{2\pi}{3}} zx)$ for e'_{2g}.